IEEE Access
Multidisciplinary ⋮ Rapid Review ⋮ Open Access Journal

Received 25 September 2023, accepted 3 October 2023, date of publication 7 November 2023,
date of current version 28 November 2023.

Digital Object Identifier 10.1109/ACCESS.2023.3330219

RESEARCH ARTICLE

GA Optimized PI-PDN Robust Control of a 1-DOF Maglev Precision Position System

HAMNA MALIK[1], SARVAT M. AHMAD[1,2], AND FAZLI WADOOD[3]

[1]Control and Instrumentation Engineering Department, King Fahd University of Petroleum and Minerals, Dhahran 31261, Saudi Arabia
[2]Interdisciplinary Research Center for Intelligent Manufacturing and Robotics, King Fahd University of Petroleum and Minerals, Dhahran 31261, Saudi Arabia
[3]Faculty of Mechanical Engineering, Ghulam Ishaq Khan Institute of Engineering Sciences and Technology, Topi 23460, Pakistan

Corresponding author: Sarvat M. Ahmad (sarvat.ahmad@kfupm.edu.sa)

The work was partly supported through Project INMR2300 at the Interdisciplinary Research Centre for Intelligent Manufacturing and Robotics, King Fahd University of Petroleum and Minerals, Dhahran, Saudi Arabia.

ABSTRACT This paper investigates 2 difficult problems encountered in magnetic levitation systems: robust control design and disturbance rejection. A PI-PDN robust control strategy is developed to control the position of a 1-degree-of-freedom (DOF) magnetic levitated rigid beam system or MLS for precision positioning applications under parametric variations, uncertainties, and external disturbances. The proposed PI-PDN gains are optimized by employing a Genetic Algorithm (GA), Marine Predator Algorithm (MPA), and Particle Swarm Optimization (PSO). GA-tuned gains lead to manifold improvement in key time and frequency domain performance specifications of rise time, settling time, overshoot, tracking error, bandwidth, classical gain, and phase margins. Additionally, the metrics of disk margins (DM) are employed for assessing the robustness of a closed-loop system subjected to simultaneous variation in gain and phase. To demonstrate the performance and effectiveness of the proposed GA-PI-PDN topology, numerical simulation results are compared with corresponding results of the benchmark PIDN with that of PI-PDN and GA-PI-PDN. The developed control algorithms were deployed on a dedicated embedded system utilizing Simulink automatic C++ code generation capabilities. The development of different control strategies was aided by building high fidelity mathematical model of electromagnets and experimental determination of important model parameters.

INDEX TERMS Magnetic levitation, precision positioning, PI-PDN controller, GA-optimization.

NOMENCLATURE

A	Electromagnetic pole face area, (m^3).
$\boldsymbol{B}$	Flux density between magnetic pole and target object, (T).
F_u	Electromagnetic force of upper electromagnet, (N).
F_l	Electromagnetic force of lower electromagnet, (N).
g	Nominal air gap between electromagnets and target object, (m).
G_c	Transfer function of controller.
$\boldsymbol{i}$	Current passing through actuator windings, (A).
I_b	Bias current, (A).
i_c	Control current, (A).
K_d	Derivative term of PID.
k_i	Force-current factor, (N/A).
K_i	Integral term of PID.
K_p	Proportional term of PID.
k_x	Force-displacement factor, (N/m).
l	Length of electromagnetic pole face, (m).
L_o	Nominal inductance, (H).
$L\,(s)$	Loop gain.
m	Mass of the PFB, (Kg).
M_S	Peak of sensitivity function, (dB).
M_T	Resonant peak, (dB).
N_t	Number of turns of electromagnetic coil.
N	Filter derivative coefficient.
$S\,(s)$	Sensitivity function.
$T\,(s)$	Complementary sensitivity function.
T_p	Peak time, (s).
T_r	Rise time, (s).
T_s	Settling time, (s).
w	Width of the electromagnetic pole face, (m).

The associate editor coordinating the review of this manuscript and approving it for publication was Su Yan.

W	stored magnetic energy, (N∗m).
x	Distance of the beam from equilibrium point, (m).
$X(s)$	Output displacement, (m).
$X^*(s)$	Reference displacement, (m).
μ_0	Permeability of air between the levitated object and electromagnets, (H/m).
ζ	Damping ratio.
α	Size of disk.
σ	Skew of disk.

I. INTRODUCTION

Magnetically levitated precision positioning systems are needed to perform micro to nanometer-scale positioning tasks in scientific instruments and manufacturing machines [1]. One state-of-the-art example of precision motion systems includes a photolithography machine [2] for the manufacturing of integrated circuits (ICs), where sub-nanometer positioning accuracy and very high speed is required. Similarly, IC inspection and packaging systems, scanning probe microscopes [3], additive manufacturing systems [4], [5], in-clean-room transportation system [6], stages for ultra-precision optical payloads [7] and precision machine tools are some other applications of precision positioning systems. Hence, the productivity and quality of the process is influenced by the motion accuracy of the maglev positioning system, and the attenuation of micro-vibrations transmitted from several disturbance sources.

Maglev is an open-loop unstable system with no damping, and reasonably fast response which makes it sensitive to external perturbations [8]. To achieve the objective of stable levitation and vibration isolation simultaneously, a controller is needed that can provide a good trade-off between reference tracking and disturbance rejection. For instance, Sun et al. [9] introduced an adaptive fuzzy cooperative control technique for the suspension system of maglev trains. The proposed approach outperformed traditional methods in terms of irregularity tracking, anti-saturation properties and cooperative capabilities, resulting in a robust system. Furthermore, steady-state error was reduced by 45% compared to Proportional Integral Derivative (PID) control while also significantly reducing overshoot and settling time. However, some residual overshoot remained despite these improvements. Sun et al. [10] also proposed a reinforcement learning-based adaptive control law, which made use of a neural network to estimate the time-varying mass and external perturbations, while a compensator was employed to eliminate the input time delay. The controller achieved an 80.5% higher accuracy compared to traditional Sliding Mode Control (SMC) when dealing with input time delays. Similarly, in literature, numerous advanced control techniques have been proposed, such as H∞ controller [11], adaptive terminal sliding mode control [12], adaptive finite-time fuzzy control [13] and hybrid adaptive feedforward internal model control [14] etc. All these controllers have complex structures which add to the computational cost. Hence, owing to its simple structure, conventional PID is still widely used. Jin et al. [15] used magnetic levitation to control the modal vibration of flexible hot galvanized steel strip in 1 DOF. He proposed a PID controller with phase compensator and tuned the compensator parameters to reduce the amplitude of 1st order bending mode, with 20 Hz frequency, by 89.2%. Shi et al. [16] combined gimbals and magnetic bearings to inertially stabilize a platform to provide a better line of sight. For low-frequency vibration estimation, he replaced displacement error with next-order error using linear extended state observer (LESO) and used a PID controller for vibration suppression. The simulations validated that this technique accelerates the convergence rate and reduces the observation error, yet there remained some overshoot. Demiroren et al. [17] magnetically levitated a ball using fractional order PID (FOPID) and tuned its parameters using an opposition based artificial electric field algorithm (ObAEF). The simulations showed that the proposed controller improved the response but still exhibited a 14.86 % overshoot. Motohiro Takahashi [18] used a PID controller in the magnetic levitation stage to achieve position accuracy in nanometers. The gains of the PID were adjusted for stability, by evaluating Nyquist plot. The gain margin of 6 dB and phase margin of 300 degrees were achieved, with a peak magnitude of 5 dB at around 100 Hz frequency. A 1-DOF PID controller structure is also extensively used at the industrial level, but as far as the highly unstable maglev process is concerned, the benchmark PID does not show satisfactory closed-loop performance. From the above references, it is perceived that PID exhibits a large overshoot due to the occurrence of dominant zeros in the closed-loop transfer function of the system. Hence, a derivative kick can be observed when there is a sudden change in the set point (and the error). Contrary to this, a 2-DOF PI-PDN controller proposed here has zeros too far from the origin, in the left half of the plane. Consequently, one can achieve a 0% overshoot. Ghosh et al. [19] levitated a ferromagnetic ball with a single electromagnet employing a 2-DOF PID controller architecture illustrating several improvements in time and frequency domain performance criteria. However, the scheme suffered from time delays due to the presence of feed-forward control which acted like a filter element for the reference signal.

A 1-DOF cantilever arm-type precision positioning actuator comprising of a combination of permanent magnet and electromagnet was devised by Kumar et al. [20] as well as by Sisodiya et al. [21] for the micro-electrical discharge machining (μ-EDM) manufacturing process. Despite its clever design, the device is similar to a ferromagnetic ball being suspended by a single electromagnet (EM). Nonetheless, the cathode tool mounted at the end of the cantilever arm is akin to a tip mass mounted at the end of a cantilever beam [22]. Wherein authors [22] developed an electromagnetic actuator for vibration control employing PID, quadratic and optimal feedback control strategies, albeit using a single EM.

The wafer inspection system, crucial in the field of semiconductor manufacturing, plays a vital role in examining wafer quality at micro to nanometer scales. Unfortunately, external vibrations from sources such as machinery or foot traffic can hinder its performance. To overcome these challenges, a novel solution has been developed: an electromagnetic levitation system. By utilizing electromagnetic forces, this system lifts the wafer stage, enabling both precise positioning and isolation from vibrations. Thus, as gleaned from the reviewed work, utilization of a single EM leads to a complex nonlinear relationship between input coil current and resulting force, giving rise to stabilization challenges.

The performance of a controller is susceptible to the fine-tuning of controller parameters. Gaikwad et al. [23] designed a PID controller for an air levitation system and optimized its gains using a Genetic Algorithm (GA). When compared with particle swarm optimization, ant colony optimization and fuzzy logic, GA showed the smallest values of objective functions based on feedback error. Zhu et al. [24] compared GA-optimized fuzzy-PID controller with simple fuzzy-PID and showed that the former one has 22.32% less regulation time, 23.29% shorter rise time and 7.18% reduced steady-state error. Barman et al. [25] demonstrated that Ziegler-Nichols (ZN) tuning technique for PID provides better outcomes when compared with conventional PID. But still, it had large settling time and rapid oscillations. To further enhance the performance, GAPID was used which resulted in minimum settling time and rise time. Ahsan et al. [26] investigated the GA-optimized PI controller and demonstrated that it outperformed the traditional root locus tuning method and meta-heuristic Marine Predator Algorithm (MPA) by as much as 22%, offering superior tracking performance with reduced control efforts.

This research aims to design a robust controller that can stabilize the 1-DOF Magnetic Levitated System (MLS) and attenuate the external vibrations concurrently by employing a pair of EMs. This work is the extension of the author's previous work on 1-DOF levitation of ferromagnetic beam [27], wherein a simple conventional PID controller was designed and implemented. However, in this work, several amendments are carried out to attain precision positioning of the pivoted-free beam, with possible utilization in precision manufacturing or similar applications. The improvements are listed below:

1) Building upon the authors' earlier work [27] and taking a cue from the 2-DOF control architecture of Ghosh et al. [19], this paper demonstrates several improvements. Notably, this research work employs a differential pair of electromagnets to levitate a ferromagnetic beam for precision positioning as opposed to a single electromagnet employed by many researchers for instance: to levitate a cantilever beam [22] for vibration control, to levitate a steel ball [17], [19], [28], [27], and in manufacturing processes [20], [21]. Utilization of a pair of EMs topology enables linearization of the force-current relationship, thereby simplifying the controller synthesis process significantly. As well as improved controller performance.
2) In here two different 2-DOF topologies are proposed, i.e., I-PDN and PI-PDN to control the coil current in the EMs. While no feedforward filter is employed unlike [19] thereby speed of response is shown to be fairly quick with no obvious time delays thus leading to improved robustness characteristics. Along with classical gain and phase margins, the metrics of disk margins (DM) are also employed for assessing the robustness of a closed-loop system subjected to simultaneous variation in gain and phase.
3) Exploiting the progress made in evolutionary algorithms such as GA, MPA and PSO the 2-DOF controller gains are tuned offline in an optimal and automated manner. Thus, the proposed 2-DOF control architecture along with the GA optimization of integral of time-weighted absolute error (ITAE) cost-function, efficiently enhances overall MLS performance as compared to the manually tuned controller designs. Including the crucial bandwidth of the MLS leading to reduced ingress of sensor noise in the closed loop.
4) Importantly, here electro-magnet parameters force-displacement and force-current factors are experimentally determined unlike in [27] for improved control design.

The paper is organized as follows: Section II presents the experimental setup and methodology. In Section III, a mathematical system model is developed, and parameters are estimated. Next in Section IV, various 2-DOF controllers are designed and implemented using Simulink due to limitations of PIDN. Bode plots of controllers for analysis are provided in Section V while the optimization problem setup, for robust controller gains, is presented in Section VI. Section VII provides a comparative analysis of the results obtained from GA, MPA, and PSO optimization techniques. Experimental validation of the controllers can be found in Section VIII. Section IX concludes the whole study.

II. EXPERIMENTAL SETUP

A CAD model of the test rig is shown in FIGURE 1. In most of the maglev configurations the vertical motion is supported by a single electromagnet. Contrary to this, a prototype of a maglev beam is developed which is stabilized between differential electromagnets. This configuration is more suitable for long-stroke applications and ensures safety as it stamps out the risk of the levitated object breaking free of the magnetic pull. The small clearance between the EMs as well as the disturbance acting on the levitated object demands fast response from the actuators for stabilizing the levitated object. The control signal for the EM actuators is a PWM signal, switching at a very high frequency of 20 kHz. The object to be levitated is a rigid beam made of ferromagnetic material and weighs 0.104 kg. The beam is pivoted at one end, and it can freely rotate about the axis passing through the pivot point, which is a frictionless pin joint. A Hall

effect sensor is used for beam displacement measurement. This magnetic sensor-based positioning of the levitated target ensures sub-micron-level accuracy [29], [30]. LAUNCHXL-F28379D microcontroller board is employed for controlling the peripherals and regulating the input and output commands in the system.

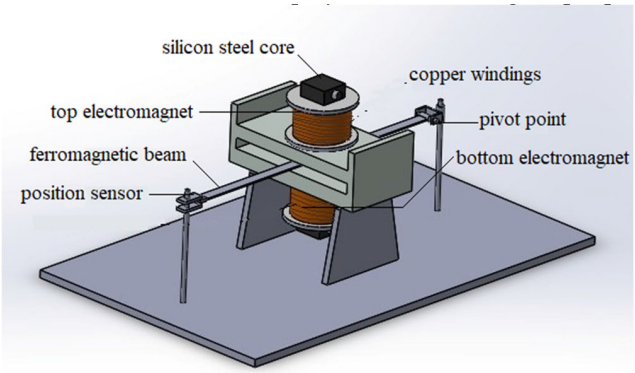

FIGURE 1. CAD model of the experimental setup.

The workflow is shown by a block diagram in FIGURE 2.

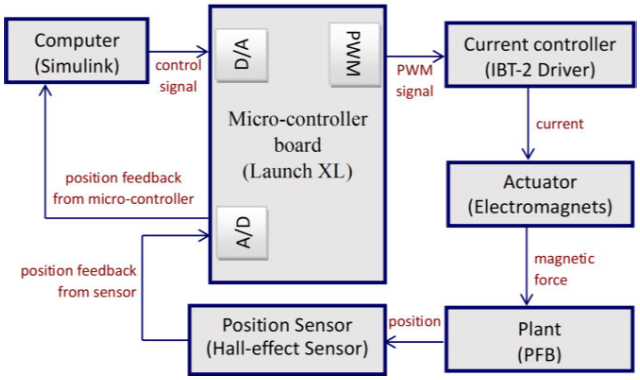

FIGURE 2. Process flow diagram.

The whole system is run through Simulink in real-time. A PWM signal command is given by Simulink to the microcontroller. It then generates a PWM signal and feeds it into the drivers which regulate the current in both upper and lower electromagnets. This current is responsible for the electromagnetic force generated by the EMs for levitating the beam. The displacement of the beam between the EMs is measured by a displacement sensor and the analog signal is fed back to the microcontroller, which is then converted into a digital signal by ADC in Simulink, and this closes the loop of the control system.

III. MATHEMATICAL MODELING

The configuration of electromagnets employed in this study is a differential-type configuration. In differential actuators the levitated object can move between a pair of actuators. Here a PFB is levitated due to applied electromagnetic forces by two I-type electromagnets mounted on both sides of the levitated object, in vertical direction, as shown in FIGURE 3. The force applied by a single I-type actuator on the levitated object is given by (1).

$$\boldsymbol{F} = \frac{\boldsymbol{B}^2 A}{2\mu_0} \tag{1}$$

where $\boldsymbol{B}$ is the flux-density of the gap between electromagnet and the levitated object, A is cross-sectional area of magnetic core and $\boldsymbol{\mu_0}$ is the permeability of air between electromagnetic actuator and beam.

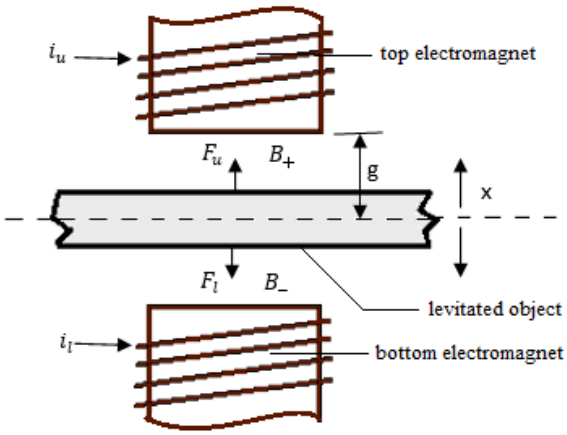

FIGURE 3. Schematic diagram of differential I-type electromagnets.

If the flux-densities for lower and upper air gaps are $\boldsymbol{B}-$ and $\boldsymbol{B}+$ then the net force applied by the electromagnets on the beam is given by (2), which is the difference between the two magnetic forces.

$$\boldsymbol{F} = \frac{A}{2\mu_0}\left(\boldsymbol{B}_+^2 - \boldsymbol{B}_-^2\right) \tag{2}$$

where $\boldsymbol{B}$ is given by,

$$\boldsymbol{B} = \frac{N_t \mu_0 \boldsymbol{i}}{2\,(g - x)} \tag{3}$$

Here N_t is the number of turns of copper winding on the inner core, $\boldsymbol{i}$ is the current passing through actuator windings, $\boldsymbol{g}$ is the air gap between actuator and the mid-point while '$\boldsymbol{x}$' is the displacement of the levitated object from mid-point of the two electromagnets. By substituting the value of $\boldsymbol{B}$ from (3) in (2), net force becomes:

$$\boldsymbol{F} = \frac{N_t^2 \boldsymbol{i}^2 \mu_0 w l}{4(g - x)^2} \tag{4}$$

At $x = 0$, when the levitated object is in the mid position, (4) reduces to (5).

$$\boldsymbol{F} = \frac{N_t^2 \boldsymbol{i}^2 \mu_0 w l}{4g^2} \tag{5}$$

Magnetic force can be expressed as a function of flux density in the air gap as well as function of inductance and current.

$$\boldsymbol{F} = \frac{L_o \boldsymbol{i}^2}{2g} \tag{6}$$

Here L_o is the nominal inductance given by (7).

$$L_o = \frac{N_t^2 \mu_o w l}{2g} \tag{7}$$

Hence, the equation of force in terms of current is given by (6).

A. LINEARIZATION OF NON-LINEAR FORCE EQUATION

Equation (4) shows that magnetic force is not linearly dependent on current and displacement. To reduce the complexity, the equation is linearized at the mid-point. The force equation shows that either current or flux density should be controlled to regulate the magnetic force. As it is easy to measure and regulate the current, a system is designed in which current is taken as input and regulated through a PWM signal.

1) FORCE CURRENT FACTOR

In (6) the current term is squared which makes the force-current relation non-linear. To linearize this relation the total current responsible for producing magnetic force through single EM is divided into two parts as follows:

$$i_u(t) = I_b + i_c(t) \tag{8}$$

$$i_l(t) = I_b - i_c(t) \tag{9}$$

Here I_b is the bias current, which is the minimum current needed to keep the object levitated. Whereas i_c is the control current which keeps fluctuating to compensate for the changes in beam position from the desired set-point. i_u and i_l is the current flowing in the upper and lower magnet, respectively. Equation (10) gives the total magnetic force F applied by differential EMs on the levitated platform i.e., the difference between force produced due to upper magnet F_u and lower magnet F_l.

$$F = F_u - F_l \tag{10}$$

By using (6) and replacing $\frac{2L_o}{g}$ by k_i', F_u and F_l can be written as:

$$F_u = \frac{k_i'}{4} i_u^2 \tag{11}$$

$$F_l = \frac{k_i'}{4} i_l^2 \tag{12}$$

substituting (8) and (9) in (11) and (12) gives (13) and (14).

$$F_u = \frac{k_i'}{4}\left(I_b^2 + i_c^2 + 2I_b i_c\right) \tag{13}$$

$$F_l = \frac{k_i'}{4}\left(I_b^2 + i_c^2 - 2I_b i_c\right) \tag{14}$$

The total magnetic force applied by differential actuators is given by (15).

$$F = k_i' I_b i_c \tag{15}$$

The above equation shows that total force is linearly related with control current, where k_i' and I_b are constant values and can be represented by a single constant given by (16).

$$F = k_i i_c \tag{16}$$

where $k_i = k_i' I_b$ and this constant is called force-current factor.

2) FORCE DISPLACEMENT FACTOR

The force given by (6) is dependent on current, where x is assumed to be zero. But when displacement is incorporated, the magnetic force becomes the non-linear function of both displacement and current. The linearization of displacement factor is done by using Taylor's series expansion of $1/g\text{-}x$ in (17).

$$\frac{1}{g-x} = \frac{1}{g\left(1 - x/g\right)} = \frac{1}{g}\left[1 + \frac{x}{g} + \left(\frac{x}{g}\right)^2 + \ldots\right] \tag{17}$$

By using above expansion, self-inductance L can be written as (18).

$$L = L_o\left[1 + \frac{x}{g} + \left(\frac{x}{g}\right)^2\right] \tag{18}$$

The magnetic energy U, stored in the coil, can be written in the form of self-inductance as (19).

$$U = \frac{1}{2} I_b^2 L_o\left[1 + \frac{x}{g} + \left(\frac{x}{g}\right)^2\right] \tag{19}$$

The partial derivative of U gives the force in (20) in terms of constant bias current as well as displacement:

$$F = \frac{dU}{dx} = 0 + \frac{L_o}{2g} I_b^2 + \frac{2x}{2g^2} I_b^2 L_o \tag{20}$$

$$F = \frac{L_o}{2g} I_b^2 + \frac{L_o}{g^2} I_b^2 x \tag{21}$$

The second term in (21) gives a linear relation of displacement of object and the force applied to levitate it, in (22).

$$F = \frac{L_o}{g^2} I_b^2 x \tag{22}$$

Total force acting on the beam from two EMs is the sum of both forces, given by (23).

$$F = \frac{2L_o}{g^2} I_b^2 x \tag{23}$$

The constant terms in the above equation can be replaced by a single constant:

$$F = k_x x \tag{24}$$

$$k_x = \frac{2L_o I_b^2}{g^2} \tag{25}$$

This constant k_x in (24) is the *force-displacement factor*. This factor is invariably positive, which makes the maglev system unstable. The net magnetic force applied on the object in terms of current and displacement factor can be written in the following form:

$$F = k_i i_c + k_x x \tag{26}$$

Equation (26) gives the linear relation of force with current and displacement.

B. EQUATION OF MOTION

The total stroke length is 8 mm which is very small, and the levitated platform is a rigid beam. Hence, a lumped parameter model can be used to represent the whole maglev system. According to the second law of motion, (26) can be expressed as (27).

$$mx'' = k_i i_c(t) + k_x x(t) \tag{27}$$

$$mx'' - k_x x(t) = k_i i_c(t) \tag{28}$$

Laplace transform of (28) gives (29).

$$ms^2 X(s) - k_x X(s) = k_i I_c(s) \tag{29}$$

Hence the transfer function of an open-loop 1 DOF maglev system is given by (30).

$$\frac{X(s)}{I_c(s)} = \frac{k_i}{ms^2 - k_x} \tag{30}$$

Model parameters are measured experimentally, where $m = 0.104$ kg, $k_x = 357$ N/m and $k_i = 10.96$ N/A. The characteristic equation is given by (31).

$$ms^2 - k_x = 0 \tag{31}$$

where $s = \pm\sqrt{\frac{k_x}{m}}$, shows that a pole of the system lies in the right half of the s-plane, which makes it unstable. Hence, a closed loop control technique is needed to stabilize the system.

IV. CONTROLLER DESIGN

The transfer function of the system indicates that it is an unstable system in open loop configuration with a pole in right-half of the s-plane. Hence, a controller is needed to control and stabilize the system. This study aims at designing a robust controller which can track the reference and attenuate the external vibrations concurrently. A conventional PID controller is first investigated acting as a benchmark, followed by two different variants i.e., I-PDN and PI-PDN controllers have been designed and implemented using Simulink-Desktop Real-Time rapid prototyping environment. The key control objectives are (i) robust stabilization of unstable plant (ii) rise time $t_r < 1.5\ sec$, settling time $t_s \sim 2\ sec$ (iii) maximum overshoot of less than 10% and (iv) closed-loop bandwidth of 3-5 Hz.

A. BENCHMARK: 1-DOF PIDN CONTROLLER

The minimum PD gains required for closed loop stabilization are derived from Routh Hurwitz criteria, according to which:

$$K_p > \frac{k_x}{k_i}, K_d > \frac{2\zeta m\sqrt{\frac{(K_p k_i - k_x)}{m}}}{k_i} \tag{32}$$

where K_p and K_d are controller gains and ζ is the damping ratio. At minimal gains, the step response is stable but has significant steady-state error. An integral with K_i gain is introduced to the controller equation to eliminate this error. However, high overshoot persists which is further reduced by fine tuning PID gains. It is imperative to monitor control efforts when utilizing the PID in practical applications to prevent saturation. The ideal derivative introduces derivative kick and allows high frequency measurement noise to enter the system. Adjusting a low pass filtered derivative coefficient N can eliminate the derivative kick and minimize the noise amplification. The block diagram of the closed loop control system with PIDN controller is shown in FIGURE 4. Equation (33) is PIDN control-law implemented on the plant.

$$G_{c-PIDN}(s) = K_p + K_i\frac{1}{s} + K_d\frac{N}{1 + N\frac{1}{s}} \tag{33}$$

The closed loop transfer function of the overall feedback system with inclusion of PIDN controller results in (34).

$$\begin{aligned} T_{PIDN} = \frac{X}{X^*} = [&\left(k_i K_p + k_i K_d N\right)s^2 \\ &+ \left(k_i K_i + k_i K_p N\right)s + k_i K_i N]/[ms^4 + Nms^3 \\ &+ \left(k_i K_p + k_i K_d N - k_x\right)s^2 \\ &+ \left(k_i K_i + k_i K_p N - k_x N\right) + k_i K_i N] \end{aligned} \tag{34}$$

Refer to the Appendix for design values of the controller. FIGURE 5(a) indicates the saturation of control efforts in transient phase, leading to 61% overshoot in step response shown in FIGURE 5(b), which highlights the necessity for an alternative control technique.

B. 2-DOF I-PDN CONTROLLER

The 2-DOF architecture comprises of two distinct controllers that operate on different inputs. Here the PDN controller is implemented as rate feedback to the plant, whereas the I controller cascaded with the plant, as shown in FIGURE 6. Contrary to the benchmark PID, the derivative term is now in the feedback path which mitigates the influence of sudden changes in set point on the control signal. Accordingly, it can be observed from FIGURE 7 that the control efforts have now been successfully contained within their saturation limits and the overshoot has been ruled out. Nevertheless, the system still exhibits a settling time of approximately three seconds. Equation (35) is the mathematical representation of closed loop system with I-PDN controller. The control parameters can be found in the Appendix section.

$$\begin{aligned} T_{I-PDN} = &[k_i K_i s + k_i K_i N]/[ms^4 + Nms^3 \\ &+ \left(k_i K_p + k_i K_d N - k_x\right)s^2 \\ &+ \left(k_i K_i + k_i K_p N - k_x N\right)s + k_i K_i N] \end{aligned} \tag{35}$$

C. 2-DOF PI-PDN CONTROLLER

PI-PDN is an alternative control technique, which employes PI and PDN controller in the forward and feedback path, respectively, as illustrated in FIGURE 8. The additional

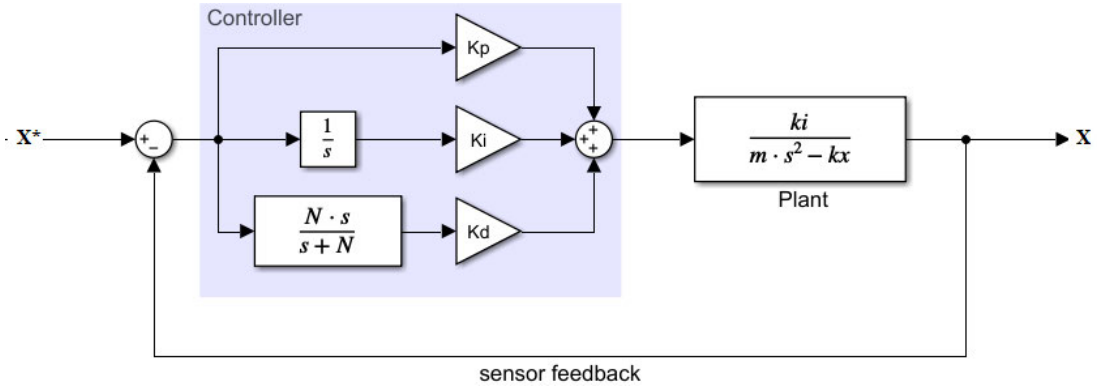

FIGURE 4. Block diagram of the closed-loop system with PIDN controller.

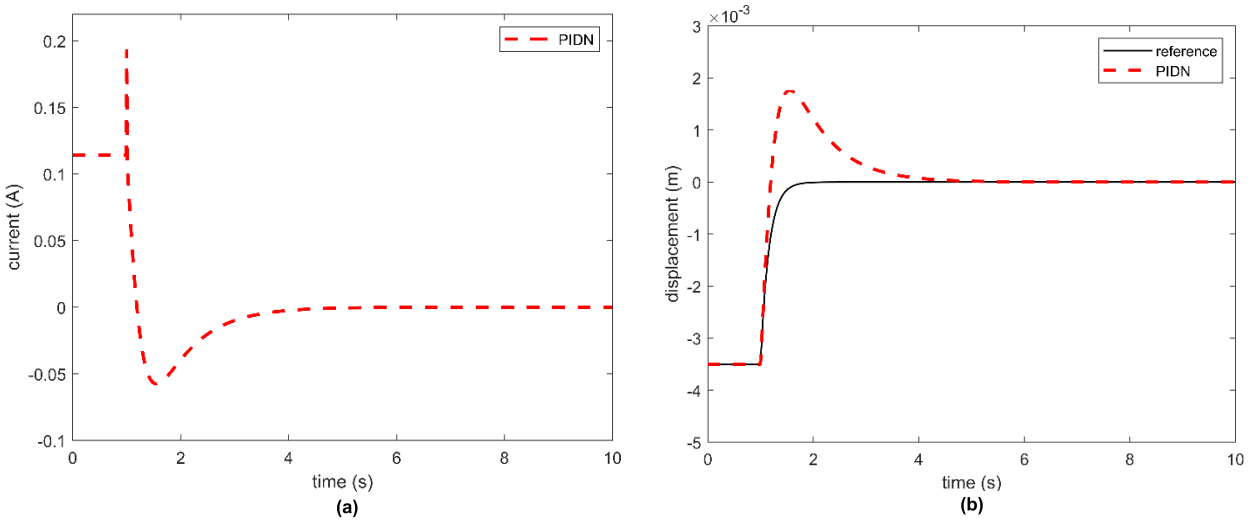

FIGURE 5. System with PIDN controller (a) Control efforts and (b) step response.

proportional component present in the PI-PDN controller offers a prompt response to variations observed in either the setpoint or disturbance. The step response of the system with PI-PDN controller in FIGURE 9, exhibits a 9-fold improvement in settling time with no occurrence of overshoot. Equation (36) is the closed loop equation of the system with PI-PDN controller. Controller gain values are given in the Appendix.

$$T_{PI-PDN} = \left[k_i K_{p1} s^2 + \left(k_i K_i + k_i K_{p1} N\right) s + k_i K_i N\right] / [ms^4 + Nms^3 + \left(k_i K_{p1} + k_i K_{p2} + k_i K_d N - k_x\right) s^2 + \left(k_i K_i + k_i K_{p1} N + k_i K_{p2} N - k_x N\right) s] \quad (36)$$

Table 1 summarizes the results obtained from time domain analysis of all three controller architectures. PI-PDN controller outperforms the other two strategies based on its fastest response rate and elimination of overshoot, with consumption of minimum control current. Equations 34-36 are employed for robustness analysis in frequency domain.

TABLE 1. Time domain performance parameters of system with PIDN, I-PDN and PI-PDN (Obtained from simulations).

Performance parameters	PIDN	I-PDN	PI-PDN
Overshoot	61%	0%	0%
Rise time (s)	0.0028	1.6	0.15
Settling time (s)	2.87	2.92	0.32
Max. i_c (A)	0.2	0.12	0.12

V. ROBUSTNESS ANALYSIS – FREQUENCY DOMAIN

To get a deeper insight into the system characteristics, its frequency domain response has been investigated. Initially, the bode plots of loop transfer function 'L' for each case are studied to determine stability margins i.e., Gain Margin (GM), Phase Margin (PM), Disk Margin (DM), Disk-based Gain Margin (DGM) and Disk-based Phase Margin (DPM). Next, complementary sensitivity function 'T' is derived and assessed for bandwidth (BW) and peak M_T. Finally, sensitivity 'S' analysis is conducted to analyze peak sensitivity M_S.

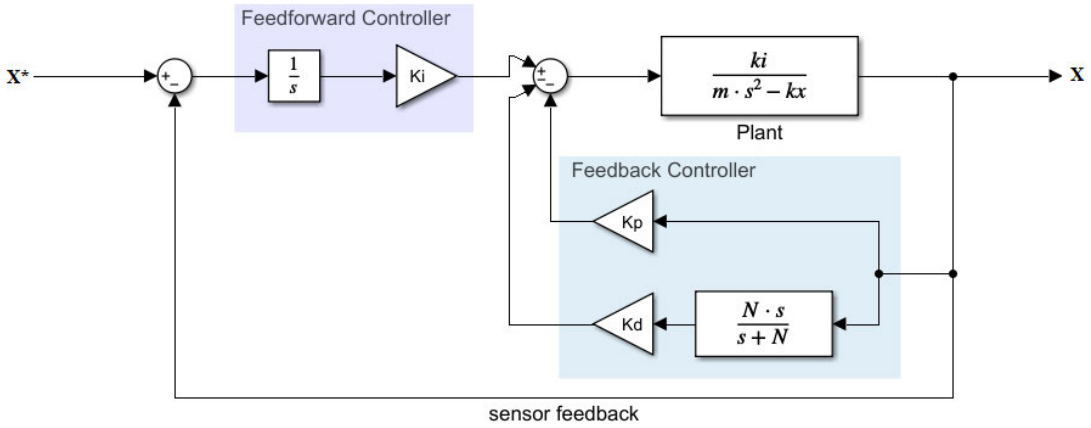

FIGURE 6. Block diagram of the closed-loop system with I-PDN controller.

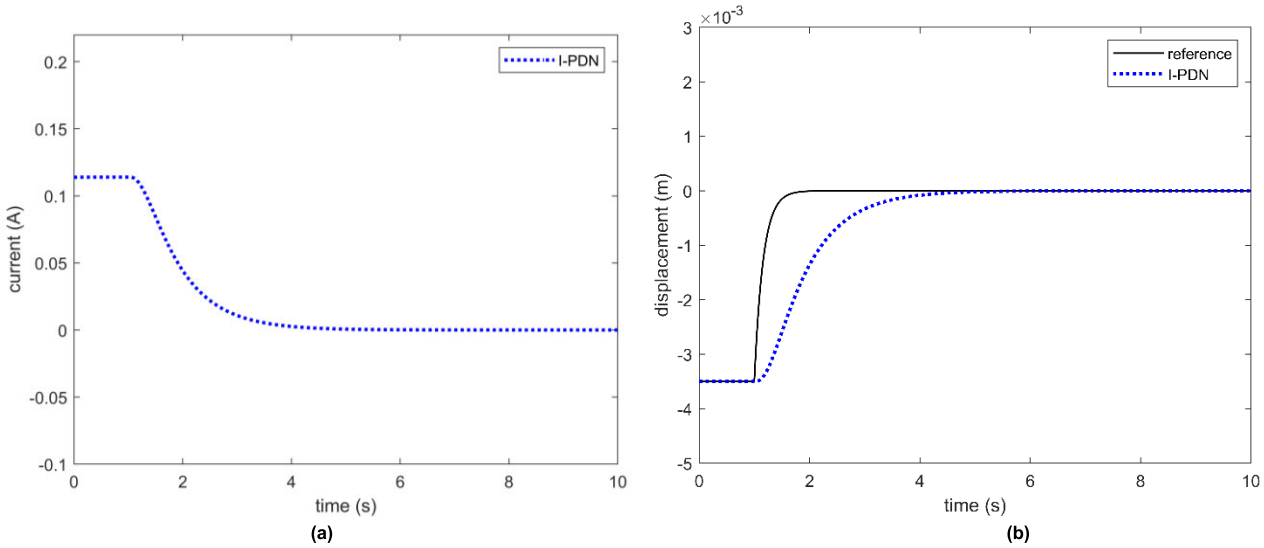

FIGURE 7. System with I-PDN controller (a) control efforts and (b) step response.

A. PIDN CONTROLLER

The bode plots of L_{PIDN}, T_{PIDN} and S_{PIDN} are presented in FIGURE 10. Equation (37) defines the loop transfer function of a system that is controlled by PIDN.

$$L_{PIDN} = \left[\left(k_i K_p + k_i K_d N\right) s^2 + \left(k_i K_i + k_i K_p N\right) s + k_i K_i N\right] / \left[ms^4 + Nms^3 - k_x s^2 - k_x Ns\right] \quad (37)$$

The gain margin is found to be -7.22 dB, which safeguards against steady state gain uncertainty. However, the margin is near 0 dB, which indicates instability. Furthermore, with a phase margin of 69.9°, the system can accommodate uncertain time-delays up to their maximum limit given by (38), without undergoing instability [31].

$$t = \frac{PM}{\omega_c} \quad (38)$$

where ω_c is the gain crossover frequency. However, it is possible for a system to have greater classical margins but is stable for a very small area in the complex plane, representing the perturbations. To uncover the potential instability regions, not evident from isolated gain and phase margins, disk margins are also taken into consideration. These margins are determined using a set of complex perturbations that consider both gain and phase variations. Each group of perturbations, labeled as $D(\alpha, \sigma)$, is represented by a disk with parameters α (size) and σ (skew). The maximum size α represents the disk margin for a particular value of σ. The robustness of a system increases as the value of disk margin and the range of DGM and DPM increase. FIGURE 13 shows the disks of all three controllers, plotted for a balanced case of $\sigma = 0$ (i.e., the maximum gain can increase and decrease by the same factor). PIDN controlled system has $\alpha = 0.8$ with DGM in the range of 0.43 to 2.3 dBs and DPM in the range of $-42.9°$ to 42.9°.

The loop transfer function can be used to obtain the corresponding sensitivity and complementary sensitivity transfer function by employing (39) and (40),

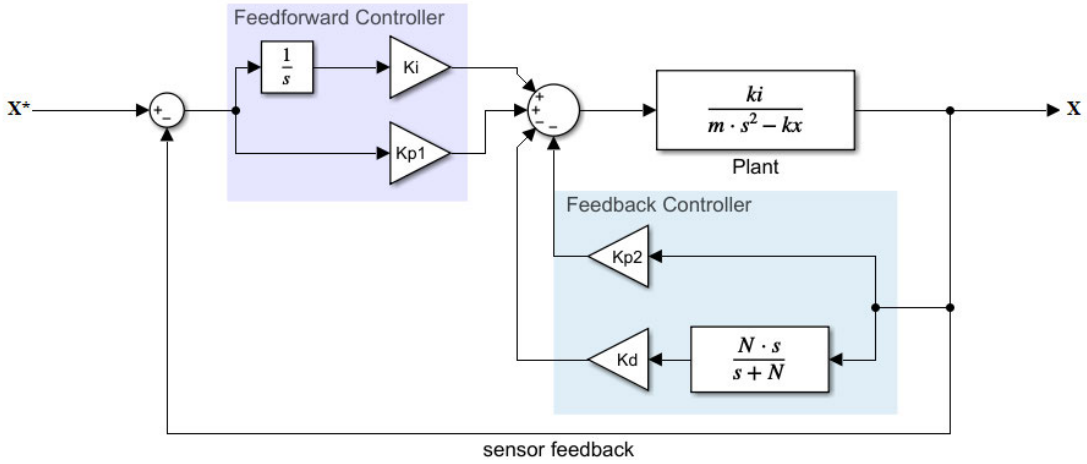

FIGURE 8. Block diagram of the closed-loop system with PI-PDN controller.

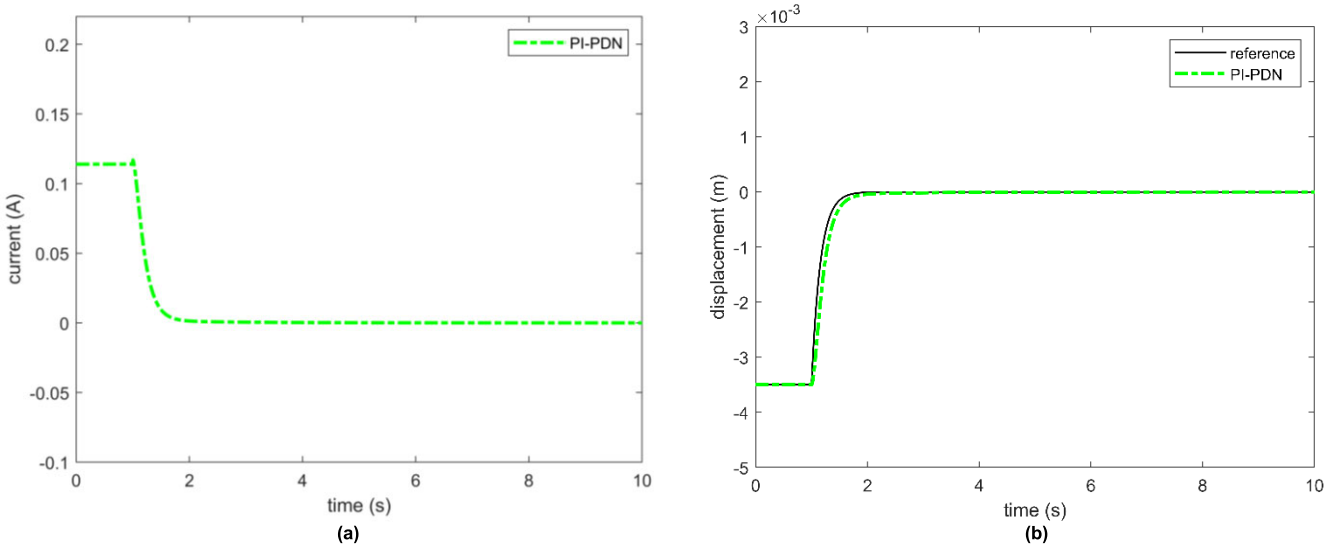

FIGURE 9. System with PI-PDN controller (a) Control efforts and (b) step response.

respectively.

$$S = \frac{1}{1+L} \tag{39}$$

$$T = \frac{L}{1+L} \tag{40}$$

The $\boldsymbol{T_{PIDN}}$ plot, acquired by utilizing (34), indicates a considerably large bandwidth of 117 Hz. Greater bandwidth will let more noise enter the system. Moreover, an unacceptable resonant peak of 4.96 dB can be detected in the low frequency region. The frequency response of $\boldsymbol{S_{PIDN}}$, mathematically represented as (41), shows $\boldsymbol{M_S}$ of 1.67 dB. A smaller value is preferable for greater robustness and disturbance rejection.

$$\begin{aligned} S_{PIDN} = &\left[ms^4 + Nms^3 - k_x s^2 - k_x Ns\right] / [ms^4 + Nms^3 \\ &+ \left(k_i K_p + k_i K_d N - k_x\right) s^2 \\ &+ \left(k_i K_i + k_i K_p N - k_x N\right) s + k_i K_i N] \end{aligned} \tag{41}$$

B. I-PDN CONTROLLER

The loop transfer function of an I-PDN-controlled system is defined by (42) and its associated bode plots are depicted in FIGURE 11.

$$\begin{aligned} L_{I-PDN} = &\left[k_i K_i s + k_i K_i N\right] / [ms^4 + Nms^3 \\ &+ \left(k_i K_p + k_i K_d N - k_x\right) s^2 + \left(k_i K_p N - k_x N\right) s] \end{aligned} \tag{42}$$

The increased disk margin, GM, and PM of 1.6, 56.7 dB and 82.2°, respectively, indicate greater robustness as compared to the PIDN controller. Moreover, the bode of $\boldsymbol{T_{I-PDN}}$ exhibits reduced bandwidth of 0.2 Hz, that can suppress the micro-vibrations contaminating the system. Also, the resonant peak has been flattened out. But, as a consequence of lowered bandwidth, the system response rate also gets retarded. $\boldsymbol{S_{I-PDN}}$ is mathematically represented by (43), shows 53% reduction in $\boldsymbol{M_S}$, which also corresponds to

enhanced robustness.

$$S_{I-PDN} = \left[ms^4 + Nms^3 + \left(k_iK_p + k_iK_dN - k_x\right)s^2 + \left(k_iK_pN - k_xN\right)s\right]/[ms^4 + Nms^3 + \left(k_iK_p + k_iK_dN - k_x\right)s^2 + \left(k_iK_i + k_iK_pN - k_xN\right)s + k_iK_iN] \quad (43)$$

C. PI-PDN CONTROLLER

The frequency response of L_{PI-PDN}, mathematically written as (44), depicted in FIGURE 12, shows that the GM and PM for PI-PDN controlled system are greatest of all previously discussed controller configurations. The disk margin is accessed to be 1.9 with $DGM = [0.02\ to\ 55.4]$ and $DPM = [-87.9\ to\ 87.9]$, which is greatest of the other two cases, further highlighting the enhanced robustness of the system.

$$L_{PI-PDN} = \left[k_iK_{p1}s^2 + \left(k_iK_i + k_iK_{p1}N\right)s + k_iK_iN\right]/[ms^4 + Nms^3 + \left(k_iK_{p1} + k_iK_dN - k_x\right)s^2 + \left(k_iK_{p1}N - k_xN\right)s] \quad (44)$$

Moreover, the T_{PI-PDN} bode plot demonstrates improved response rate, but at the cost of broader bandwidth. However, as the bandwidth is still within the required frequency range of micro-vibrations, the PI-PDN controller seems to result in a good tradeoff between response rate and noise rejection. The sensitivity transfer function is given by (45). Further reduction of 91% in M_S can be observed from its frequency response in FIGURE 12.

$$S_{PI-PDN} = [ms^4 + Nms^3 + \left(k_iK_{p1} + k_iK_dN - k_x\right)s^2 + \left(k_iK_{p1}N - k_xN\right)s]/[ms^4 + Nms^3 + \left(k_iK_{p1} + k_iK_{p2} + k_iK_dN - k_x\right)s^2 + \left(k_iK_i + k_iK_{p1}N + k_iK_{p2}N - k_xN\right)s] \quad (45)$$

Table 2 summarizes the frequency domain performance parameters of all three controllers. Based on the analysis conducted, it is evident that the PI-PDN controller exhibits remarkable performance. This can be attributed to its notable robustness and ability to withstand disturbances without compromising system stability. Moreover, the bandwidth of this controller falls well within the required range, further validating its effectiveness in achieving desired outcomes.

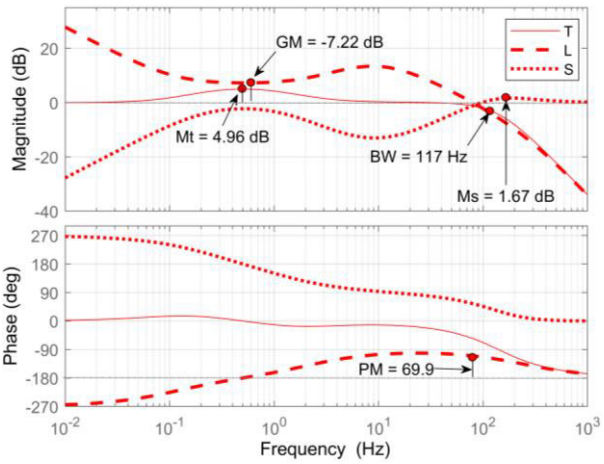

FIGURE 10. T, L and S bode plots of PIDN controlled system (Simulated).

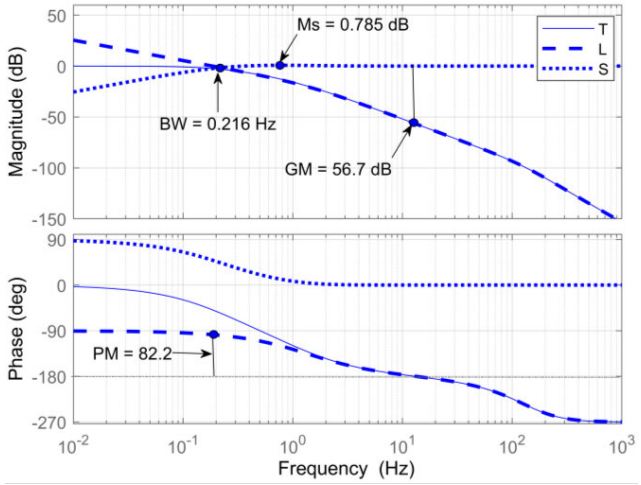

FIGURE 11. T, L and S bode plots of I-PDN controlled system (Simulated).

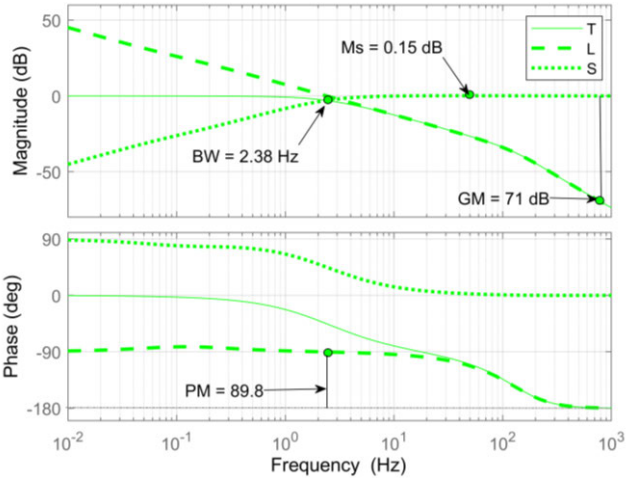

FIGURE 12. T, L and S bode plots of PI-PDN controlled system (Simulated).

VI. OPTIMIZATION OF PI-PDN GAINS

Among the three control architectures, PI-PDN has shown the best performance. Therefore, its gains are further refined by employing three different offline, AI (Artificial Intelligence) tuning algorithms, namely the Genetic Algorithm (GA), Marine Predator Algorithm (MPA) and Particle Swarm Optimization (PSO). These algorithms combine population-based heuristics and iterative processes inspired by nature to navigate complex solution spaces. By leveraging the strengths of these algorithms, this study aims to

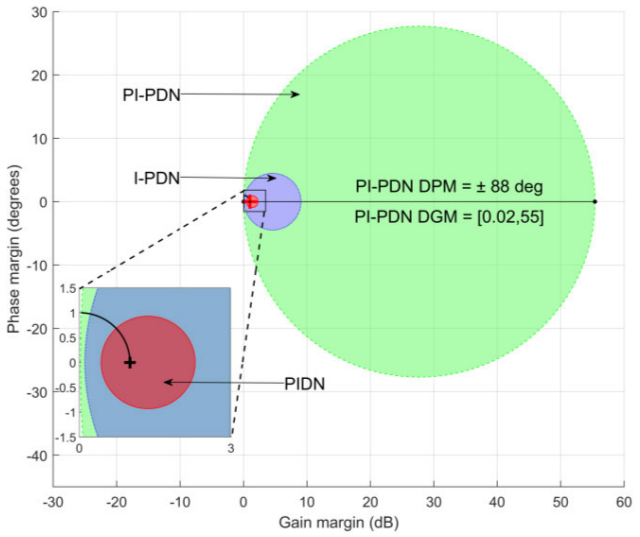

FIGURE 13. Disk margin plot of PIDN, I-PDN and PI-PDN (Simulated).

TABLE 2. Frequency Domain Performance Parameters of System with PIDN, I-PDN and PI-PDN (Obtained from Simulations).

Performance parameters	PIDN	I-PDN	PI-PDN
Gain margin (dB)	-7.22 (At 0.503 Hz)	56.7 (At 13.2 Hz)	71 (At 815 Hz)
Phase margin (deg)	69.9 (At 79.3 Hz)	82.2 (At 0.18 Hz)	89.8 (At 2.39 Hz)
Disk margin	0.8	1.6	1.9
DGM (dB)	0.43 - 2.29	0.11 - 9.06	0.02 - 55.4
DPM (deg)	-42.9 - 42.9	-77.4 - 77.4	-87.9 - 87.9
Bandwidth (Hz)	117	0.216	2.38
M_T (dB)	4.96	-	-
M_S (dB)	1.67	0.785	0.15

improve stability, precision, and robustness of the control system.

A. GA PROBLEM SETUP

Genetic Algorithm (GA) is a metaheuristic optimization tool, originated from the process of natural selection which drives biological evolution. The algorithm starts by initializing the chromosomes. For the PI-PDN based control, the set of chromosomes comprises of five tuning parameters K_{p1}, K_i, K_d, N and K_{p2}. Bounds are set for the K_{p1}, K_i, K_d and K_{p2} gain values based on Routh Hurwitz Criteria, and for the filtered-derivative coefficient N considering the Fast Fourier Transform of the feedback signal. The lower limit for N is selected such that the system does not get unstable due to the significant time-delay added as a consequence of small cut-off frequency. While the upper constraint is chosen to avoid the contamination of system response with undesirable noise.

The next step is to create an initial population of individual designs. The algorithm uses a uniform random number generator to create the initial population. The population size is selected based on the number of decision variables, problem complexity and computational resources. However, as a rule of thumb, the population size should be at least 10 times the number of decision variables. Hence, for the current optimization problem, the initial population size is set to 50 for 5 variables. The population creation is succeeded by the selection of an objective function. The objective function is a fitness function that gives a fitness value corresponding to the chromosomes. The quality of the individual solution is measured based on its fitness function value. Hence, choosing an appropriate fitness function is a crucial step for acquiring an optimal solution. Here, the GA based optimization is intended to minimize the objective function given by (46), which is the Integral of Time-weighted Absolute Error (ITAE) value of the controller parameters.

$$ITAE = \int t\,|e\,(t)|\,dt \tag{46}$$

where e is the error given by difference of reference step signal and the step response of transfer function at time t. The closed loop transfer function is given by (47):

$$\begin{aligned} T_{PI-PDN} &= \left[k_i K_{p1} s^2 + \left(k_i K_i + k_i K_{p1} N\right) s + k_i K_i N\right] / [ms^4 + Nms^3 \\ &\quad + \left(k_i K_{p1} + k_i K_{p2} + k_i K_d N - k_x\right) s^2 \\ &\quad + \left(k_i K_i + k_i K_{p1} N + k_i K_{p2} N - k_x N\right) s] \end{aligned} \tag{47}$$

Next step is the selection of potentially effective solution. In this problem, the stochastic universal sampling (SUS) technique is used for this purpose. In this technique the individuals are mapped on a continuous line and the length of the line segments corresponds to the fitness value. The selection is done through equally spaced pointers placed over the line. Just one random value is used in this technique, for determining the position of the first pointer.

New individuals are generated from the selected parents through mating, which is executed by means of crossover and mutation. The population evolves over successive generations and provides an optimal solution. The algorithm stops if it meets the termination criteria, otherwise the process is repeated. In this case, the GA provided the optimized gains ($K_{p1} = 36.25, K_i = 61.3, K_d = 2.35, N = 1384$ and $K_{p2} = 36.5$) in 40 iterations with the objective function value of 1.4e-5. The stepwise execution of genetic algorithm for estimation of optimized PI-PDN gains is demonstrated in FIGURE 14.

B. MPA PROBLEM SETUP

The Marine Predator Algorithm is an innovative optimization method that draws inspiration from the foraging patterns of marine predators as they search for food. During interactions between marine predators and prey, predators employ a scavenging strategy known as Brownian and Lévy random movement. Predators use the Brownian method when there is a high concentration of prey in the hunting area, while

they utilize the Lévy method when prey concentration is low. However, environmental factors such as eddy formation or fish aggregating devices [FAD] can influence the behavior of marine predators. In terms of search space, FAD effects are trapping phenomena resembling local optima points. According to natural selection principles, individuals with superior fitness within the population are chosen as exclusive members and represented in an elite matrix for further optimization purposes [32]. The execution steps for optimization can be visualized in the flowchart in FIGURE, and the key parameters associated with it are provided in Table 3.

TABLE 3. MPA Setup Parameters.

Parameters	Value
Number of preys	50
Cost function	ITAE
Upper bounds $[K_{p1}, K_i, K_d, N, K_{p2}]$	[32, 0, 0, 700, 32]
Lower bounds $[K_{p1}, K_i, K_d, N, K_{p2}]$	[100, 100, 5, 2000, 100]
Dimensions	5
Termination criteria	Tolerance = 1e-6

C. PSO PROBLEM SETUP

The particle swarm optimization algorithm takes inspiration from the swarming behavior of birds or insects. Each particle in the population is attracted to both its personal best location and the best location found by any member of the swarm. Over time, the population can converge on one or a few optimal locations or continue exploring.

To start, initial particles are created, and velocities are assigned. The objective function is evaluated at each particle's current location to determine their individual best value $\boldsymbol{P_{best}}$ and corresponding location. New velocities are then calculated based on factors such as current velocity, individual best locations of particles, and neighboring particle's best locations, to determine globally best position i.e., $\boldsymbol{G_{best}}$. This process continues iteratively, until stopping criteria is met, with updates made to particle positions (by adding velocities while ensuring they remain within bounds), velocities, and neighbors [33].

The flowchart in FIGURE outlines the steps for executing optimization, while Table 4 provides important parameters related to it. In the PSO algorithm, the balance between personal and global knowledge utilization in a particle is influenced by cognitive and social coefficients ($\boldsymbol{c_1}$ and $\boldsymbol{c_2}$). The velocity updates of particles are guided by the adaptive inertia range, which determines trade-offs between exploration and exploitation. The coefficient values are determined empirically based on their impact on exploration and exploitation dynamics, fine-tuned through experimentation for effective convergence.

TABLE 4. PSO Setup Parameters.

Parameters	Value
Swarm size	50
Cost function	ITAE
Upper bounds $[K_{p1}, K_i, K_d, N, K_{p2}]$	[32, 0, 0, 700, 32]
Lower bounds $[K_{p1}, K_i, K_d, N, K_{p2}]$	[100, 100, 5, 2000, 100]
Dimensions	5
$\mathbf{c_1}$	1.49
$\mathbf{c_2}$	1.49
Adaptive inertia range	0.1 - 1.1
Termination criteria	Tolerance = 1e-6

VII. COMPARATIVE ANALYSIS OF OPTIMIZATION TECHNIQUES

In this section a comprehensive analysis of the three algorithms is done in both frequency and time domain. The algorithms are executed multiple times with a variety of parameters to ensure reliability and to avoid premature convergence. The outcomes are compared, to pick the most optimal ones (see Appendix) for implementation on the physical setup.

A. TIME DOMAIN ANALYSIS

The controller optimized using the GA demonstrates a smoother performance without any overshoot and minimum current consumption, with a maximum value of 0.24 A. It settles quickly with an efficient response time ($T_r = 0.134$ s and $T_s = 0.24$ s), indicating its effectiveness in optimization compared to PSO and MPA algorithms. Although the PSO and MPA algorithms result in slightly shorter response times, they come at the expense of overshoot and nearly double current consumption. Through analysis of the time domain step response in FIGURE 18 and corresponding current efforts showcased in FIGURE 17, it can be concluded that GA is a more effective optimization technique when compared to PSO and MPA methods.

B. FREQUENCY DOMAIN ANALYSIS

After analyzing the L, T, and S bode plots of GA, MPA and PSO optimized controllers in FIGURE 19, FIGURE 20 and FIGURE 21, respectively, it becomes apparent that the Genetic Algorithm has proven to be superior to the other two algorithms. The GA exhibits greater stability margins ($GM = 70.5$ dB and $PM = 87°$) compared to its counterparts. Notably, with a bandwidth of 2.6 Hz, it offers effective low frequency vibration isolation capabilities. Moreover, achieving a small value of M_S i.e., 0.34 dB ensures minimal sensitivity towards external disturbances. The frequency and time domain performance parameters of

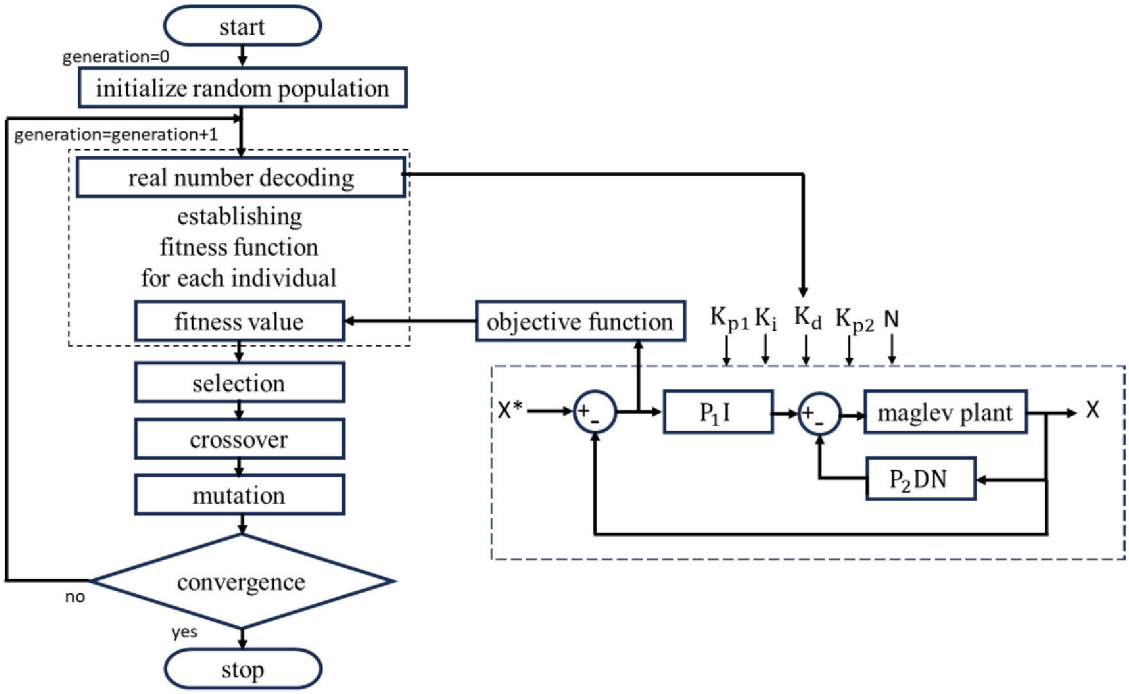

FIGURE 14. Flow chart of genetic algorithm.

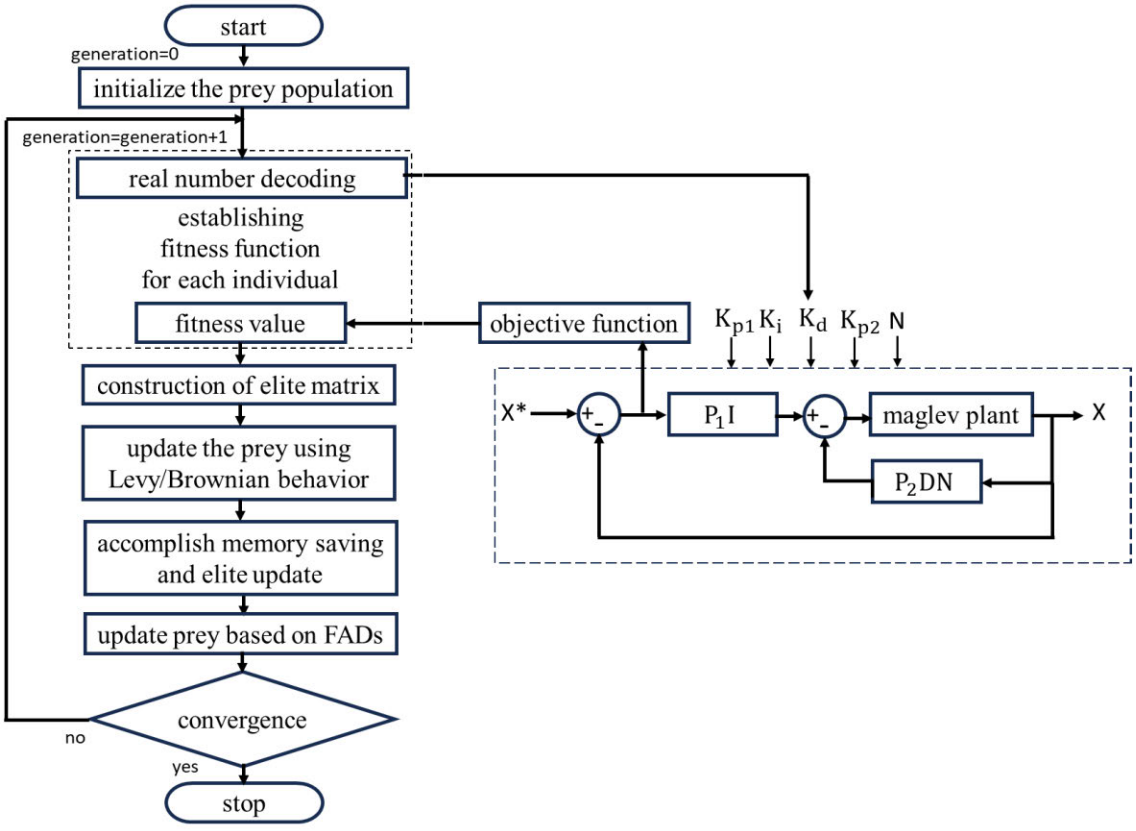

FIGURE 15. Flowchart of marine predator algorithm.

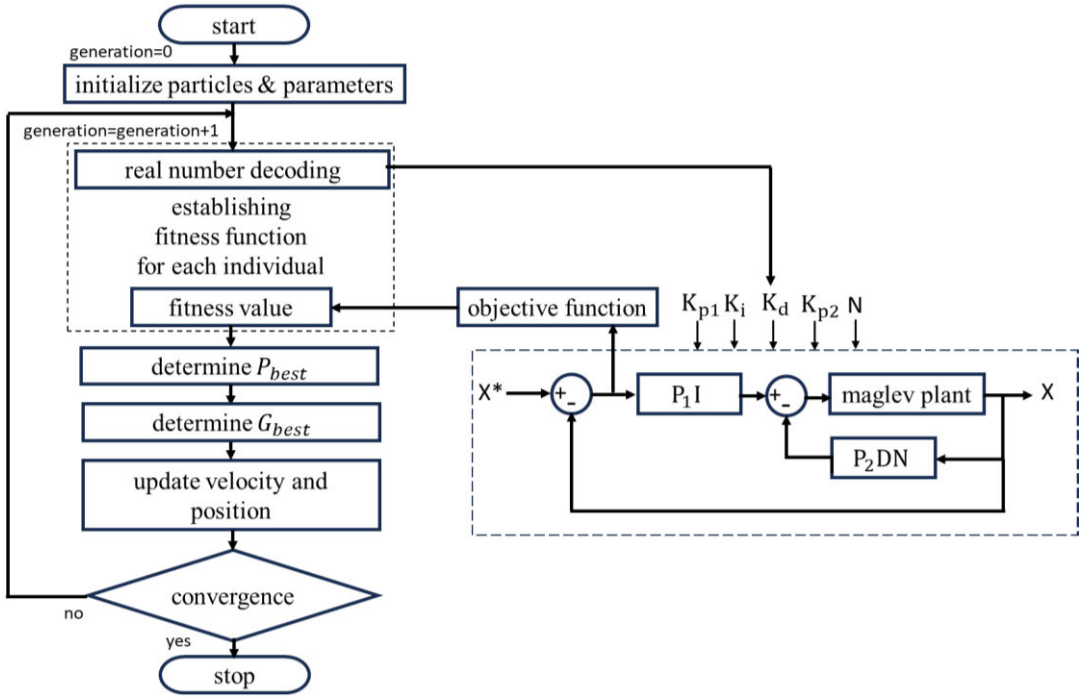

FIGURE 16. Flow chart of particle swarm optimization algorithm.

all three optimization techniques are compiled in Table 5 for comparison.

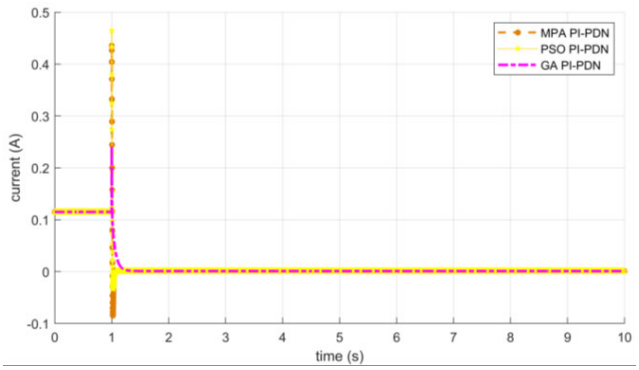

FIGURE 17. Simulated control efforts of MPA, PSO and GA optimized PI-PDN controllers.

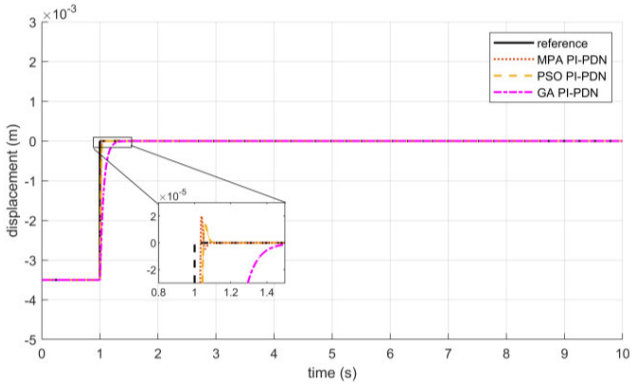

FIGURE 18. Simulated step response of MPA, PSO and GA optimized PI-PDN controlled system.

VIII. EXPERIMENTAL RESULTS

The actual test-rig is shown in FIGURE 22. The control is implemented through Simulink-Desktop Real-Time. A constant bias current $I_b = 0.124$ A, is added to the controller output, hence the control effort is only the compensating control current i_c. A Butterworth filter has also been designed to filter out the high frequency noise from the position sensor input.

A. PERFORMANCE ANALYSIS IN TIME DOMAIN

Both transient and steady state step responses for PIDN, I-PDN and PI-PDN controlled system can be observed and compared from FIGURE 23, FIGURE 24 and FIGURE 25, respectively. Following results can be deduced from it:

1) %OS: an over-shoot of 54% can be observed only in the case of the PIDN controller. It dies out in the other two cases due to rate feedback.
2) Settling time: I-PDN shows the slowest rate of response with a rise time of 0.8 s. The other three controllers have a satisfactory rate of response with PIDN being the fastest. But it takes more time to settle, hence GA PI-PDN is more considerable due to its shortest settling time.
3) Noise cancellation: I-PDN and GA PI-PDN exhibit the smoother response on account of the shorter bandwidth. Contrary to this, PIDN has the largest

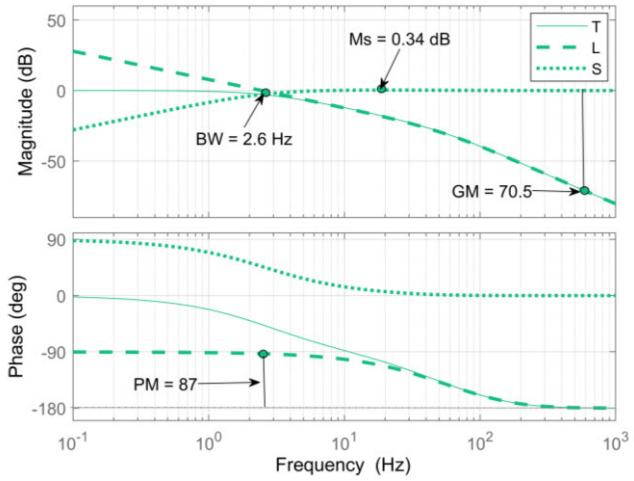

FIGURE 19. T, L and S bode plots of GA PI-PDN system (Simulated).

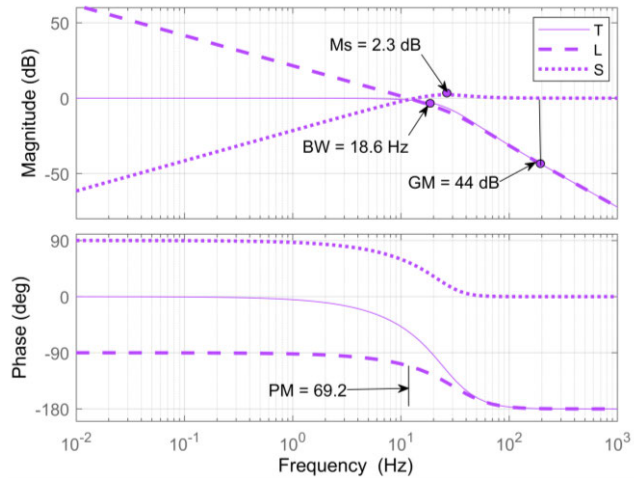

FIGURE 20. T, L and S bode plots of MPA PI-PDN system (Simulated).

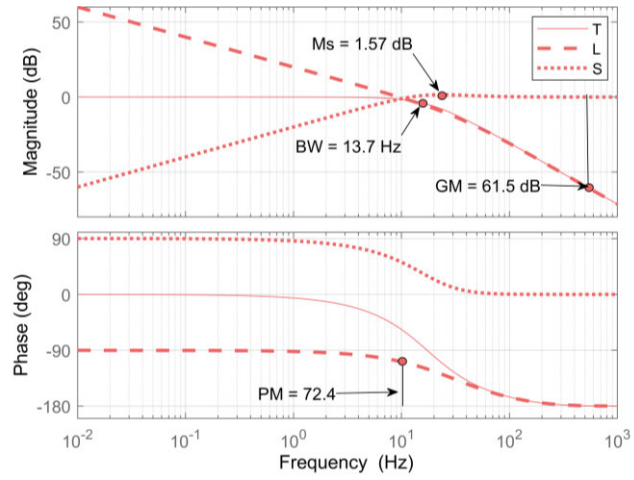

FIGURE 21. T, L and S bode plots of PSO PI-PDN system (Simulated).

bandwidth and hence it lets more noise enter the system and contaminates the response.

TABLE 5. Performance parameters of system with GA, PSO and MPA optimized PI-PDN controller (Obtained from simulations).

Performance parameters	GA	MPA	PSO
Overshoot	0%	.604%	.39%
Rise time (s)	0.134	0.0187	0.025
Settling time (s)	0.24	0.03	0.04
Max. i_c (A)	0.24	0.43	0.46
Gain margin (dB)	70.5 (at 578 Hz)	44 (at 191 Hz)	61.5 (at 555 Hz)
Phase margin (deg)	87 (at 2.46 Hz)	69.2 (at 11.6 Hz)	72.4 (at 9.9 Hz)
Bandwidth (Hz)	2.6	18.6	13.7
M_T (dB)	0	1.09e4	1.09e4
M_S (dB)	0.34	2.3	1.57

From these observations it can be concluded that GA PI-PDN is the most robust solution among all.

FIGURE 26 shows the control efforts for all the three cases. GA PI-PDN puts the minimum control effort for stabilization. On the other hand, PIDN results in maximum noise and control efforts with the current saturating at the lower side. The current range for the physical system is from $0-0.73$ A, while the PIDN control efforts go as below as -0.2 A. I-PDN is between the two extremes.

TABLE 6. Time domain performance parameters of system with PIDN, I-PDN and GA PI-PDN controller.

Performance parameters	PIDN	IPDN	GA PI-PDN
Overshoot	54%	0%	0%
Rise time (s)	0.084	1.03	0.14
Settling time (s)	2.77	3.41	0.29
Max. i_c (A)	0.42	0.27	0.25

Table 6 summarizes the time and frequency domain performance parameters for all three controllers. The time domain analysis validates the simulations and emphasizes the superior performance of GA PI-PDN.

1) REFERENCE TRACKING AND DISTURBANCE REJECTION

GA optimized PI-PDN controller is further investigated for reference tracking and disturbance rejection. This time a multi-step position reference is given at the input. FIGURE 27 shows that the controller is making the system track the reference quite well, for the entire range of inputs.

To analyze how well the controller rejects the disturbance, the system is perturbed with an impulse of -16 N/s, 24 N/s and 36 N/s for 0.05 s, as shown in FIGURE 28.

From FIGURE 29 it can be noticed that the system quickly reverts to the reference position in less than a second.

Moreover, FIGURE 30 shows that the controller immediately responds to the external disturbance and provides compensation for it by regulating i_c, without getting saturated.

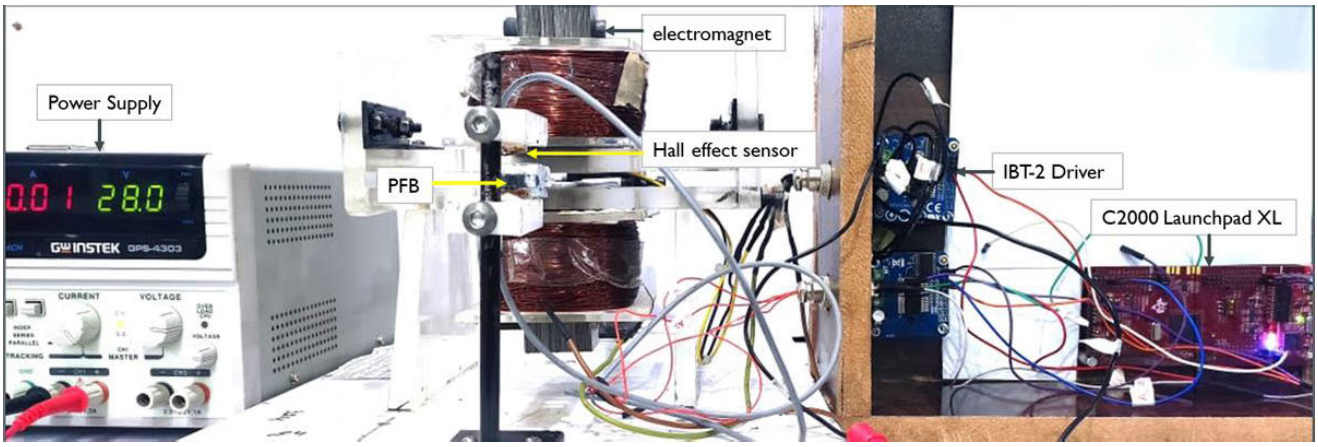

FIGURE 22. Experimental setup.

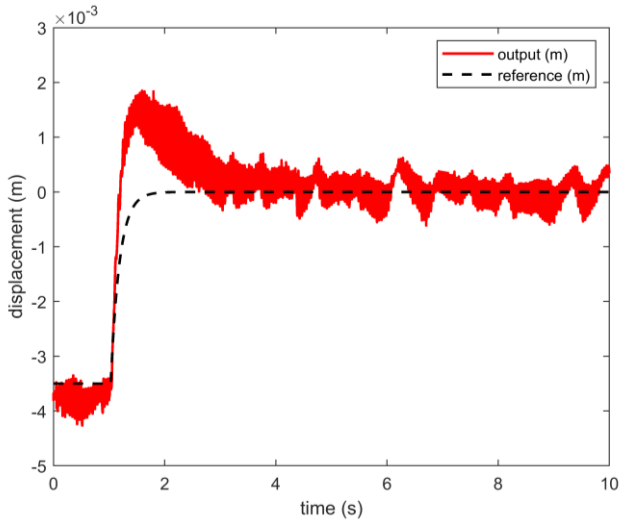

FIGURE 23. Experimental step response of system with PIDN.

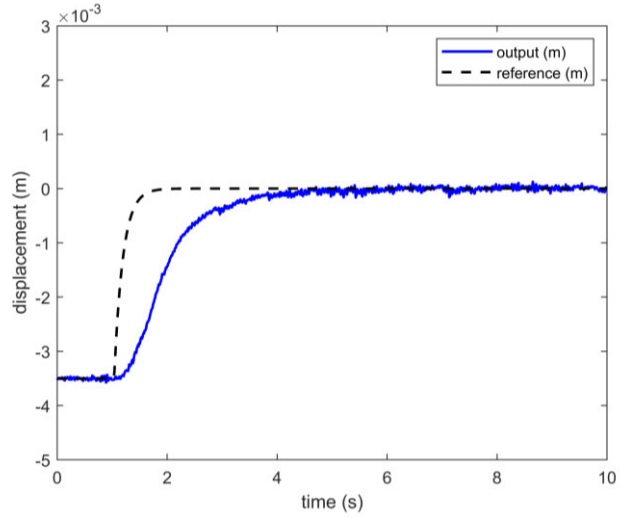

FIGURE 24. Experimental step response of system with I-PDN.

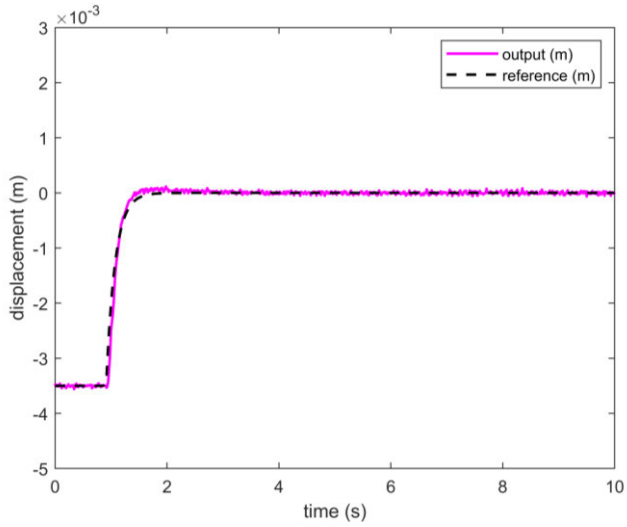

FIGURE 25. Experimental step response of system with GA PI-PDN.

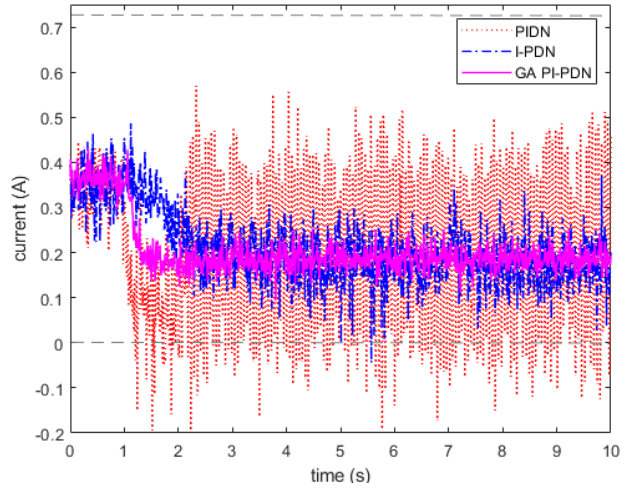

FIGURE 26. Experimental control efforts of PIDN, I-PDN and GA-PI-PDN controllers.

From Table 7, it is evident that the actual results for GA PI-PDN closely align with those obtained from simulations. This observation serves as validation for our model's accurate representation of system dynamics. The similarity further

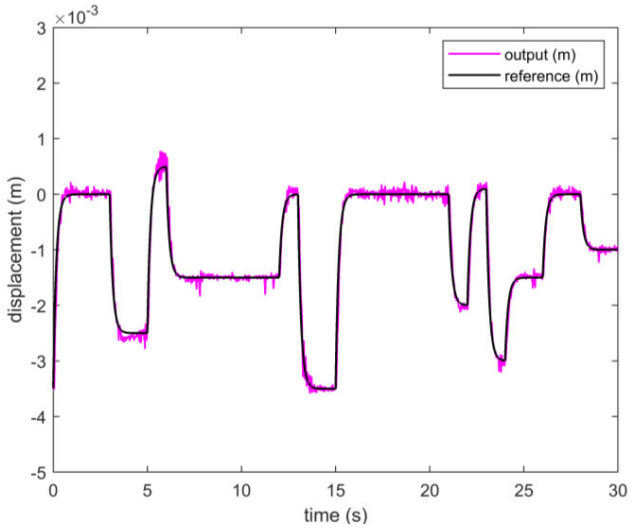

FIGURE 27. Reference tracking with GA PI-PDN controller.

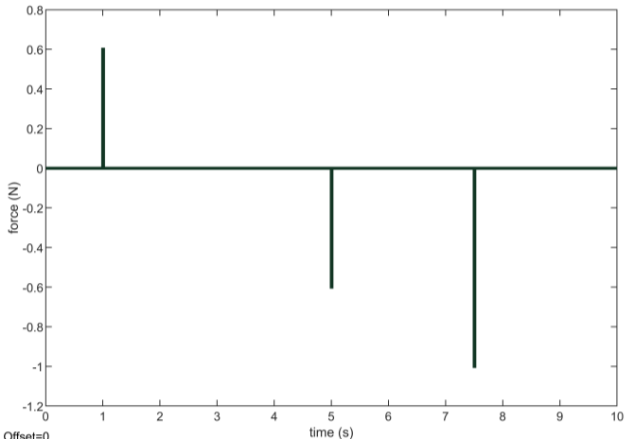

FIGURE 28. Input disturbance.

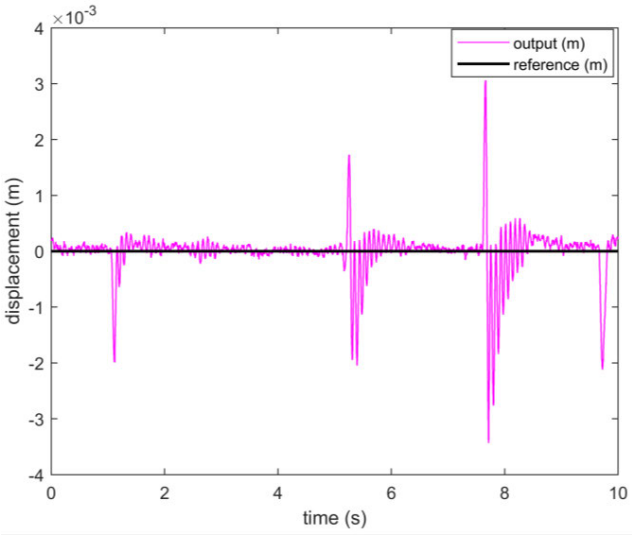

FIGURE 29. Disturbance rejection with GA PI-PDN controller.

emphasizes the efficacy of using genetic algorithms for parameter tuning. Therefore, it can be argued that GA

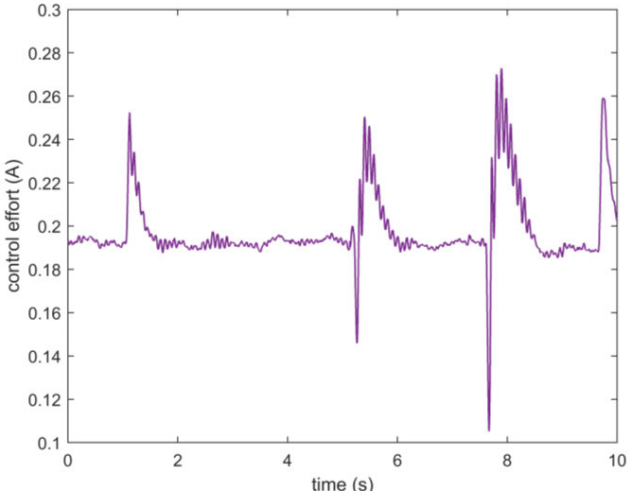

FIGURE 30. GA PI-PDN controller response to external disturbance.

TABLE 7. Comparative analysis of performance parameters of simulated and experimental system with GA PI-PDN controller.

Performance parameters	GA PI-PDN (Simulation)	GA PI-PDN (Experimentation)	% difference
Overshoot	0%	0%	0 %
Rise time (s)	0.134	0.14	4.3 %
Settling time (s)	0.24	0.29	4.0 %
Max. i_c (A)	0.24	0.25	4.1 %

PI-PDN control methodology excels in managing uncertain and unmodeled variables as well as time lags compared to the two alternative techniques.

IX. CONCLUSION

This paper dealt with the development of high-fidelity mathematical models of electro-magnetic circuits deployed for levitating ferromagnetic beams referred as precision positioning systems. The paper delves into the design and analysis of robust control strategies namely PI-PDN, employing a pair of electromagnets which simplifies the complex nonlinearity issue arising in such systems. Consequently, this strategy effectively addresses related stabilization challenges with successful elimination of overshoot, and 88% reduction in response rate, when compared to PIDN control method. Additionally, there was a notable 40% decrease in current consumption and a 2.4-fold increase in disk margin with drastic reduction in sensitivity by 91%. This control algorithm is further improved upon using Genetic Algorithm, Marine Predator Algorithm and Particle Swarm Optimization techniques. Nonetheless, GA-tuned PI-PDN was found to be superior for precise positioning of the tip of the beam on which the sensor is likely to be mounted. The proposed controllers have a 2 degrees-of-freedom architecture as opposed to a single loop of the benchmark PIDN controller, accruing several performance benefits. The simulations and experimental results demonstrate that

GA-PI-PDN outperforms the PIDN and PI-PDN in terms of both time and frequency domain required performance characteristics. That is in terms of rise time, settling time, no tracking error, robustness (gain margin, phase margin, parameter variation and disturbance rejection, disk margin, disk-based gain margin, disk-based phase margin) and crucial closed-loop bandwidth and (attenuated) noise-free control efforts requirement. The efficacy of the robust algorithms was successfully demonstrated in real-time on the test-rig interfaced with Simulink Desktop Real-Time and data acquisition card. The results exhibited similarity of approximately 96% with those obtained from simulations. This work is a precursor to future research on 2 degrees-of-freedom magnetic levitation of precision platform/positioning system.

ACKNOWLEDGMENT

The authors would like to thank the King Fahd University of Petroleum and Minerals, and the deanship of research oversight and coordination for their assistance and support. The work was partly supported through Project INMR2300.

APPENDIX

Table 8 compiles the controller gains of all the controllers implemented in this article.

TABLE 8. Controller gains.

	K_p	K_i	K_d	N
PIDN	75	50	5	1500
I-PDN	75	50	5	1500
PI-PDN	75, 37	50	5	1500
GA PI-PDN	36.25,36.5	61.3	2.35	1384
MPA PI-PDN	91.5, 33.2	50	1.2	352
PSO PI-PDN	100, 33	23.7	1.6	1596

REFERENCES

[1] L. Zhou and J. Wu, "Magnetic levitation technology for precision motion systems: A review and future perspectives," *Int. J. Autom. Technol.*, vol. 16, no. 4, pp. 386–402, Jul. 2022, doi: 10.20965/ijat.2022.p0386.

[2] W. J. Kim, D. L. Trumper, and J. B. Bryan, "Linear motor-leviated stage for photolithography," *CIRP Ann.*, vol. 46, no. 1, pp. 447–450, 1997, doi: 10.1016/S0007-8506(07)60862-2.

[3] T. Ou, C. Hu, Y. Zhu, M. Zhang, and L. Zhu, "Intelligent feed-forward compensation motion control of maglev planar motor with precise reference modification prediction," *IEEE Trans. Ind. Electron.*, vol. 68, no. 9, pp. 7768–7777, Sep. 2021, doi: 10.1109/TIE.2020.3013795.

[4] P. Kumar, S. Malik, E. Toyserkani, and M. Khamesee, "Development of an electromagnetic micromanipulator levitation system for metal additive manufacturing applications," *Micromachines*, vol. 13, no. 4, p. 585, Apr. 2022, doi: 10.3390/mi13040585.

[5] P. Kumar, Y. Huang, E. Toyserkani, and M. B. Khamesee, "Development of a magnetic levitation system for additive manufacturing: Simulation analyses," *IEEE Trans. Magn.*, vol. 56, no. 8, pp. 1–7, Aug. 2020, doi: 10.1109/TMAG.2020.2997759.

[6] M. Futamura and S. Ohata, "Rail magnet arrangements for improved stability of a superconducting transport system," *IEEE Trans. Appl. Supercond.*, vol. 32, no. 6, pp. 1–5, Sep. 2022, doi: 10.1109/TASC.2022.3167929.

[7] Z. Gong, L. Ding, H. Yue, H. Gao, R. Liu, Z. Deng, and Y. Lu, "System integration and control design of a maglev platform for space vibration isolation," *J. Vib. Control*, vol. 25, no. 11, pp. 1720–1736, Apr. 2019, doi: 10.1177/1077546319836892.

[8] A. S. C. Roong, C. Shin-Homg, and M. A. B. Said, "Position control of a magnetic levitation system via a PI-PD control with feedforward compensation," in *Proc. 56th Annu. Conf. Soc. Instrum. Control Eng. Jpn. (SICE)*, Sep. 2017, pp. 73–78, doi: 10.23919/SICE.2017.8105536.

[9] Y. Sun, H. Qiang, L. Wang, W. Ji, and A. Mardani, "A fuzzy-logic system-based cooperative control for the multi-electromagnets suspension system of maglev trains with experimental verification," *IEEE Trans. Fuzzy Syst.*, vol. 31, no. 10, pp. 3411–3422, Mar. 2023, doi: 10.1109/TFUZZ.2023.3257036.

[10] Y. Sun, J. Xu, C. Chen, and W. Hu, "Reinforcement learning-based optimal tracking control for levitation system of maglev vehicle with input time delay," *IEEE Trans. Instrum. Meas.*, vol. 71, pp. 1–13, Jan. 2022, doi: 10.1109/TIM.2022.3142059.

[11] B. C. Yalçın and K. Erkan, "3-DoF zero power micro vibration isolation via linear matrix inequalities based on H∞ and H_2 control approaches," *Mech. Syst. Signal Process.*, vol. 153, May 2021, Art. no. 107506, doi: 10.1016/j.ymssp.2020.107506.

[12] H. M. S. Yaseen, S. A. Siffat, I. Ahmad, and A. S. Malik, "Nonlinear adaptive control of magnetic levitation system using terminal sliding mode and integral backstepping sliding mode controllers," *ISA Trans.*, vol. 126, pp. 121–133, Jul. 2022, doi: 10.1016/j.isatra.2021.07.026.

[13] T. Zhang, S. Jiang, D. Shen, and H. Xu, "Adaptive finite-time fuzzy control for hybrid levitation system of maglev trains with active anti-lock constraints," *J. Franklin Inst.*, vol. 360, no. 4, pp. 2635–2659, Mar. 2023, doi: 10.1016/j.jfranklin.2023.01.006.

[14] Z. Gong, L. Ding, S. Li, H. Yue, H. Gao, and Z. Deng, "Payload-agnostic decoupling and hybrid vibration isolation control for a maglev platform with redundant actuation," *Mech. Syst. Signal Process.*, vol. 146, Jan. 2021, Art. no. 106985, doi: 10.1016/j.ymssp.2020.106985.

[15] C. Jin, F. Xiong, Z. Bao, Y. Xu, and L. Xu, "Research on modal vibration suppression of maglev steel strip based on phase compensator," *J. Sound Vib.*, vol. 434, pp. 78–91, Nov. 2018, doi: 10.1016/j.jsv.2018.07.043.

[16] W. Shi, K. Liu, and W. Zhao, "Active vibration isolation of a maglev inertially stabilized platform based on an improved linear extended state observer," *IEEE Access*, vol. 9, pp. 743–751, 2021, doi: 10.1109/ACCESS.2020.3046886.

[17] A. Demirören, S. Ekinci, B. Hekimoğlu, and D. Izci, "Opposition-based artificial electric field algorithm and its application to FOPID controller design for unstable magnetic ball suspension system," *Eng. Sci. Technol., Int. J.*, vol. 24, no. 2, pp. 469–479, Apr. 2021, doi: 10.1016/j.jestch.2020.08.001.

[18] M. Takahashi, "Design concept and structural configuration of magnetic levitation stage with Z-assist system," *Int. J. Autom. Technol.*, vol. 15, no. 5, pp. 706–714, Sep. 2021, doi: 10.20965/ijat.2021.p0706.

[19] A. Ghosh, T. Rakesh Krishnan, P. Tejaswy, A. Mandal, J. K. Pradhan, and S. Ranasingh, "Design and implementation of a 2-DOF PID compensation for magnetic levitation systems," *ISA Trans.*, vol. 53, no. 4, pp. 1216–1222, Jul. 2014, doi: 10.1016/j.isatra.2014.05.015.

[20] D. Kumar, M. S. Sisodiya, D. K. Mandal, and V. Bajpai, "Maglev micro-EDM: Feasibility and performance on inconel 625," *CIRP J. Manuf. Sci. Technol.*, vol. 40, pp. 155–166, Feb. 2023, doi: 10.1016/j.cirpj.2022.11.012.

[21] M. S. Sisodiya, S. Shukla, and V. Bajpai, "Feasibility analysis of novel maglev EDM by comparing with conventional micro EDM," *Sci. Rep.*, vol. 12, no. 1, Feb. 2022, Art. no. 2613, doi: 10.1038/s41598-022-06662-1.

[22] R.-F. Fung, Y.-T. Liu, and C.-C. Wang, "Dynamic model of an electromagnetic actuator for vibration control of a cantilever beam with a tip mass," *J. Sound Vib.*, vol. 288, nos. 4–5, pp. 957–980, Dec. 2005, doi: 10.1016/j.jsv.2005.01.046.

[23] D. P. Gaikwad, B. S. Patil, and L. S. Patil, "Advance genetic algorithm-based PID controller for air levitation system," *Int. J. Model., Identificat. Control*, vol. 41, no. 3, pp. 243–255, Dec. 2022, doi: 10.1504/ijmic.2022.127519.

[24] Z. Zhu, Y. Liu, Y. He, W. Wu, H. Wang, C. Huang, and B. Ye, "Fuzzy PID control of the three-degree-of-freedom parallel mechanism based on genetic algorithm," *Appl. Sci.*, vol. 12, no. 21, p. 11128, Nov. 2022, doi: 10.3390/app122111128.

[25] A. Barman, S. Dutta, K. Tiwari, S. Roy, and S. Pain, "Genetic algorithm based adaptive PID tuning of time delay process," in *Proc. Int. Symp. Artif. Intell.* Cham, Switzerland: Springer, Feb. 2022, pp. 64–75.

[26] A. Tanveer and S. M. Ahmad, "High fidelity modelling and GA optimized control of yaw dynamics of a custom built remotely operated unmanned underwater vehicle," *Ocean Eng.*, vol. 266, Dec. 2022, Art. no. 112836, doi: 10.1016/j.oceaneng.2022.112836.
[27] M. R. Siddiqui, S. M. Ahmad, and U. Asghar, "Stabilizing control of a 1-DOF electromagnetic levitation of pivoted-free rigid ferromagnetic beam," *Measurement*, vol. 106, pp. 35–45, Aug. 2017, doi: 10.1016/j.measurement.2017.03.028.
[28] A. V. Starbino and S. Sathiyavathi, "Design of sliding mode controller for magnetic levitation system," *Comput. Electr. Eng.*, vol. 78, pp. 184–203, Sep. 2019, doi: 10.1016/j.compeleceng.2019.07.007.
[29] H. Yu and W.-J. Kim, "A compact Hall-effect-sensing 6-DOF precision positioner," *IEEE/ASME Trans. Mechatronics*, vol. 15, no. 6, pp. 982–985, Dec. 2010, doi: 10.1109/TMECH.2010.2050003.
[30] H. J. Ahn and K. R. Kim, "2D Hall sensor array for measuring the position of a magnet matrix," *Int. J. Precis. Eng. Manuf.-Green Technol.*, vol. 1, no. 2, pp. 125–129, Apr. 2014, doi: 10.1007/s40684-014-0017-0.
[31] S. Skogestad and I. Postlethwaite, "Classical feedback control," in *Multivariable Feedback Control: Analysis and Design*, 2nd ed. Hoboken, NJ, USA: JWS, 2001, ch. 2, sec. 2.4.3, pp. 32–33.
[32] A. Tanveer and S. M. Ahmad, "Cross-coupled dynamics and MPA-optimized robust MIMO control for a compact unmanned underwater vehicle," *J. Mar. Sci. Eng.*, vol. 11, no. 7, p. 1411, Jul. 2023, doi: 10.3390/jmse11071411.
[33] Sumit, R. Shukla, and A. K. Sinha, "Study of PID controller gain for active vibration control using FEM based particle swarm optimization in COMSOL multiphysics," *J. Micromanufacturing*, vol. 6, no. 1, pp. 40–49, May 2023, doi: 10.1177/25165984221086439.

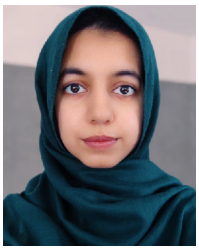

HAMNA MALIK received the B.S. degree in mechatronics and control engineering from the University of Engineering and Technology, Faisalabad, in 2020, and the M.S. degree in mechanical engineering from the GIK Institute of Engineering Sciences and Technology, Swabi, in 2023. She is currently pursuing the Ph.D. degree with the Control and Instrumentation Engineering Department, King Fahd University of Petroleum and Minerals, Saudi Arabia. From 2020 to 2023, she was a Research Assistant with the Vibration Dynamics and Controls Laboratory. Her research interests include data-driven modeling and the control of maglev systems.

SARVAT M. AHMAD received the Ph.D. degree from the Department of Automatic Control and Systems Engineering, The University of Sheffield, U.K., in May 2001.

He has held postdoctoral positions with the University of Plymouth and The University of Manchester, U.K. He is a Chartered Engineer of IMechE, U.K., who after working for several years in cutting edge mechatronics industries in the U.K. returned to academia. Currently, he is an Associate Professor with the Control and Instrumentation Engineering Department, King Fahd University of Petroleum and Minerals, Saudi Arabia. To date, he has authored or coauthored more than 50 journals and conference papers. His research interests include dynamics, system identification and robust control with application to unmanned aerial vehicles, unmanned underwater vehicles, and active magnetic bearings. He was a recipient of the prestigious Denny Medal awarded by the Institute of Marine Engineering, Science and Technology, U.K., in 2010, for the article titled "Pure pursuit guidance and model predictive control of an autonomous underwater vehicle for cable/pipeline tracking."

FAZLI WADOOD received the D.A.E. degree in electronics engineering from the Government College of Technology, Quetta, in 2008. From 2009 to 2010, he was an Electronics Technician with PAK TECH TELECOM. From 2010 to 2017, he was a Laboratory Technician with Fast National University. Since 2017, he has been a Laboratory Technician with the Vibration Dynamics and Controls Laboratory, Ghulam Ishaq Khan Institute of Engineering Sciences and Technology, Swabi. He has assisted in more than ten research projects. He has technical skills of PCB designing and instrumentation. His research interests include the design and development of remotely operated vehicles and maglev systems.